WARWICK
THE UNIVERSITY OF WARWICK

warwick.ac.uk/lib-publications

Capacity fade modelling of lithium-ion battery under cyclic loading conditions

T.R Ashwin[a,*], Y. M. Chung[a,**], J. Wang[a]

[a]*School of Engineering, University of Warwick, Coventry, CV4 7AL, UK*

Abstract

A pseudo two-dimensional (P2D) electro-chemical lithium-ion battery model is presented in this paper to study the capacity fade under cyclic charge-discharge conditions. The Newman model [1, 2] has been modified to include a continuous solvent reduction reaction responsible for the capacity fade and power fade. The temperature variation inside the cell is accurately predicted using a distributed thermal model coupled with the internal chemical heat generation. The model is further improved by linking the porosity variation with the electrolyte partial molar concentration, thereby proving a stronger coupling between the battery performance and the chemical properties of electrolyte. The solid electrolyte interface (SEI) layer growth is estimated for different cut-off voltages and charging current rates. The results show that the convective heat transfer coefficient as well as the porosity variation influences the SEI layer growth and the battery life significantly. The choice of an electrolyte decides the conductivity and partial molar concentration, which is found to have a strong influence on the capacity fade of the battery. The present battery model integrates all essential electro-chemical processes inside a lithium-ion battery under a strong implicit algorithm, proving a useful tool for computationally fast battery monitoring system.

Keywords: Lithium-ion battery, electrochemical model, capacity fade, ageing model, thermal model, battery management system

---

*Present address: WMG, University of Warwick
**Corresponding Author
Email address: Y.M.Chung@warwick.ac.uk (Y. M. Chung)

1. Introduction

A battery management system (BMS) is an essential part of hybrid electric vehicles (HEV), plug-in electric vehicles (PEV), and also large-scale grid support systems. Also the demand for portable devices and electronic communication systems has accelerated the need for more focussed research in batteries and battery packs. The lithium-ion battery is a popular choice for battery packs due to its high energy density, relatively low self-discharge, low maintenance, and suitability for high current applications. The use of battery packs in grid support applications presents several challenges due to the rapid charge and discharge demanded by grid operation which may cause unexpected failure that can potentially lead to catastrophic damage to the batteries and bring the impact on to grid. A continuous monitoring of an individual battery is critical to the smooth grid operation and the estimation of remaining useful life (RUL) of the battery.

The success of a battery monitoring algorithm greatly depends on the accurate prediction of electro-chemical parameters, capacity fade and thermal characterisation. Capacity fade and the prediction of electro-chemical characteristics are linked to the battery operating conditions. The thermal heat generation is also highly complicated to characterise due to its dependency on multiple electro-chemical reactions. Electro-chemical modelling using partial differential equations can predict battery characteristics accurately, but with a high computational cost. This poses a main challenge for accurate battery modelling and emphasises the need to focus more on electro-chemistry as well as numerical schemes for an accurate and computationally fast monitoring system. This paper analyses the dependency of main factors such as temperature, depth of discharge (DoD) and the charging current rate on the SEI layer development. This study also improves the solution methods under an implicit algorithm to solve the electro-chemical effects in battery, making it as a useful tool for battery life monitoring.

There were early attempts to model the electro-chemical processes inside the battery by solving the governing equations using a pseudo two-dimensional model, known as the P2D model [1, 2]. Later, Wang *et al.* [3] and Subramani *et al.* [4] approximated the concentra-

tion of solid particles of a P2D model using a second degree polynomial and improved the speed of calculation with an accuracy comparable to the P2D model. Dao *et al.* [5] and Bizeray *et al.* [6] modelled the basic electrochemistry inside the battery using mathematical simplification and reduction methods to improve the computational speed. These models enable a computationally fast solution of the problem, leading to an accurate estimation of battery parameters, which is extremely useful in battery monitoring systems. However, these mathematical methods are not accurate enough to predict the capacity fade coupled with thermal effects in a battery during multiple charge-discharge cycles.

Capacity fade modelling is very important for an accurate prediction of charge-discharge profiles in rechargeable battery RUL prediction. It has been observed that side reactions and degradation process in lithium-ion batteries may cause a number of undesirable effects, leading to capacity loss and the growth of the solid electrolyte interface (SEI) layer, which are normally salt degradation products of electrolyte and electrodes [7, 8]. The loss of lithium ions contributes to the thickening of the SEI layer at the negative electrode, initially protecting the electrode against large voltage but eventually degrading the capacity. The actual process of capacity fade happens over hundreds of cycles while some batteries exhibit rapid degradation, strongly influenced by adverse operating conditions.

A detailed solvent diffusion model was proposed by Ploehn at al. [8] to evaluate the growth of the SEI layer in carbon anodes. Later, Ramadass *et al.* [9] developed a first principle based model to calculate the capacity fade effect by considering a continuous solvent reduction side reaction. Recently, Pinson and Bazant [10] showed that simple time dependent models were capable of predicting the capacity fade in electro-chemical batteries. The accuracy of these models depends on the numerical schemes and the calculation of heat generation inside the battery. Further improvement has been made to the battery modelling by Randall *et al.* [11] and by Tanim and Rahn [12].

An accurate thermal prediction is required to calculate capacity fade, since high heat generation is the main reason for accelerated capacity and power fade leading to uncontrollable side reactions. This also helps the engineers design a better battery cooling mechanism

which enhances the battery life. Most of early thermal prediction studies were based on the lumped parameter approach, representing a battery as a large thermal mass without considering internal thermal conductivity [13]. Later, Wu *et al.* [14] extended the study of Smith and Wang [13] for a battery pack with interconnected resistance focusing on the load imbalance generated in automobile applications. In the lumped model, thermal properties are averaged, which reduces the accuracy of thermal prediction.

A distributed thermal model provides high accuracy thermal predictions at a high computational cost. One of the important attempts was made by Cai and White [15], extending the P2D model to include the thermal effect using COMSOL software. Attempts were made to improve the accuracy of distributed thermal model by extending it to multi-dimensions and length scales with the help of a reduced order model to limit the computational cost [16]. Ye *et al.* [17] experimentally determined accurate thermal modelling parameters and used it in simulation, and their results showed good agreement with test data.

Another notable study from our group on lithium-ion polymer battery was by Chacko and Chung [18] on thermal behaviour of cell during the combination of charge and discharge effect, using a three-dimensional fully coupled electro-chemical model. There is an experimental effort by Barai *et al.* [19] to characterise Li-ion batteries. Also other major contributions are by Yi *et al.* [20] and Kim et al. [21].

All the above studies point to the necessity of capturing three different effects such as electro-chemical reaction [13], capacity fade or power fade leading to ageing [9], and thermal effects that governs temperature distribution [15]. A strong and computationally fast battery life monitoring system also needs an accurate and fast numerical scheme or algorithm for solving the governing equations. Variable porosity also needs to be given due importance above the three factors to accurately calculate the available specific area which directly affects the system of equations [22].

The present study predicts the basic electro chemistry inside the battery using a pseudo two-dimensional (P2D) model. This study also takes into account the heat generation inside the battery as well as the capacity fade and power fade due to solvent reduction reaction. A

variable porosity model is introduced by linking the reactions with the partial molar volume. Hence this electro-chemical model is an attempt to capture the electro-chemistry, capacity fade, and its coupled effects with temperature. The implementation of a computationally fast and robust algorithm makes this model suitable for BMS with high numerical accuracy. A finite volume based discretisation is adopted due to the inherent advantage that the boundary conditions can be applied non-invasively. An algorithm is proposed which sequentially solves the governing equations using an implicit method for time dependent discretisation, to evaluate the battery characteristics for multiple charge-discharge cycles.

2. Battery Model

A Li-ion battery has typically three major components, namely, current collectors, porous electrodes and ionically conductive separator. This layout was first presented by Fuller *et al.* [23]. Later this modelling layout was widely adopted [13, 9, 15]. The negative composite electrode is made of active material of LiC_6 and the positive electrodes is made of metal oxide active material such as $LiMO_2$. The electrolyte is made of organic solvents or lithium salts such as $LiPF_6$ which promotes the ionic diffusion process. The P2D model assumes that the electrodes can be represented by the lattice of spherical particles of identical size. The surface concentration of each spherical particle is used to determine stoichiometry for calculating the open circuit potential (OCV).

During the discharge process, positive lithium ions from the negative electrode diffuse towards the positive electrode. The reverse electrochemical process occurs during the charge process, and the SEI layer consumes some of these lithium ions at the negative electrode leading to the thickening of the layer.

2.1. Governing equations

All governing equations and boundary conditions used in this study are given in this section. The basic electro-chemical battery model is based on Smith and Wang [13]. The capacity fade model is based on Ramadass *et al.* [9]. The distributed thermal model energy equation and the convective boundary conditions are based on Cai and White [15]. The

5

distributed model thermal properties are taken from the experimental work of Maleki *et al.*[24]. The porosity change is directly linked to the partial molar concentration following Sikha *et al.* [22]. A graphical illustration of the present model is presented in Figure 1a, and all parameters used are shown in Table 1.

2.1.1. Li^+ ions in the electrolyte phase

Conservation of Li in the electrolyte phase relates the time variation of Li-ion with its diffusion in the electrolyte. The electrolyte phase Li concentration, c_e, is given by the following equation.

$$\frac{\partial}{\partial t}(\varepsilon_e c_e) = \nabla \cdot (D_{e,eff} \nabla c_e) + \frac{1 - t^+}{F}(J_1 + J_s). \tag{1}$$

The effective diffusion coefficient is evaluated by $D_{e,eff} = D_e \varepsilon_e^P$, where ^{P} is the Bruggeman porosity exponent. Li-ion cannot diffuse through the current collectors. Thus the boundary condition at the two ends of battery is given by:

$$\left.\frac{\partial c_e}{\partial x}\right|_{x=0} = 0, \quad \left.\frac{\partial c_e}{\partial x}\right|_{x=L} = 0.$$

2.1.2. Li^+ ions in the solid phase

Conservation of Li in the solid phase is described by Fick's law of diffusion. The solid phase Li concentration, c_s, is a function of its axial position x and its radial position r; *i.e.* $c_s(x, r, t)$.

$$\frac{\partial}{\partial t}c_s = \frac{D_s}{r^2}\frac{\partial}{\partial r}\left(r^2 \frac{\partial}{\partial r}c_s\right). \tag{2}$$

At the sphere surface,

$$-D_s \left.\frac{\partial c_s}{\partial r}\right|_{r=\Lambda_s} = \frac{J_1}{a_s F}.$$

At the centre of spherical particle, the concentration gradient is set to zero.

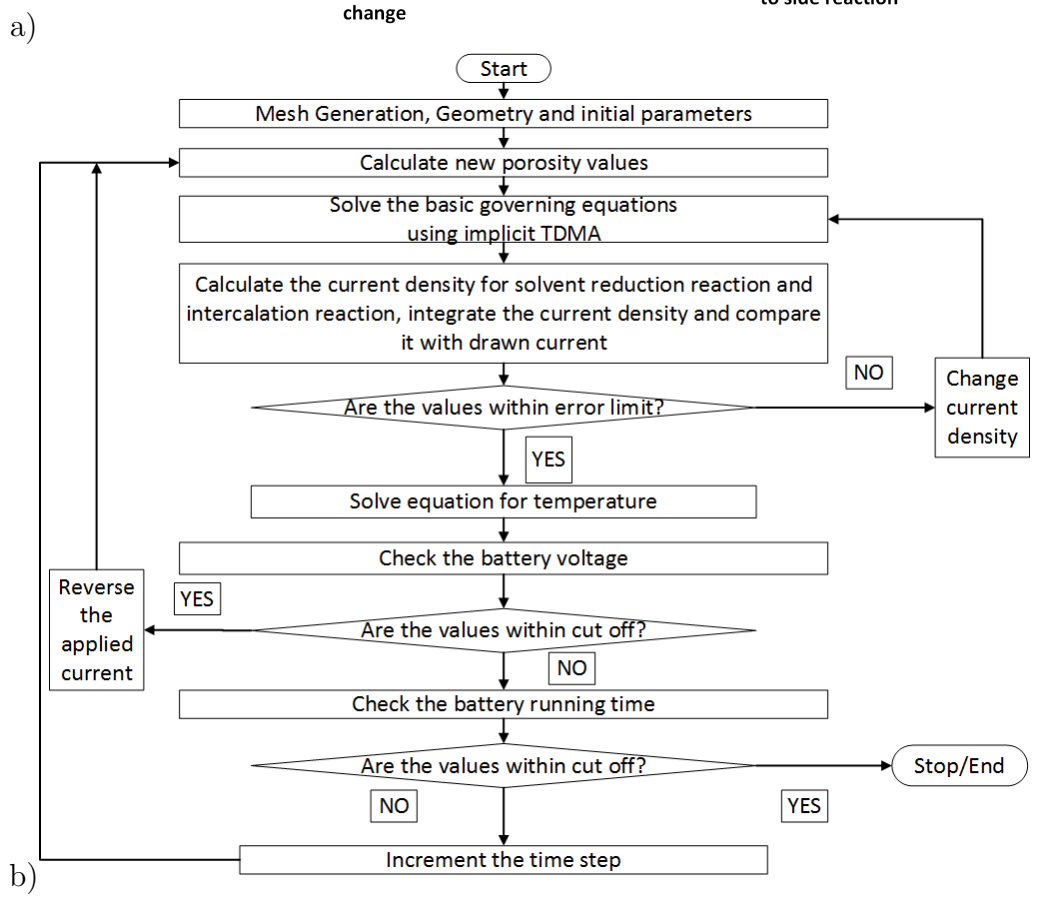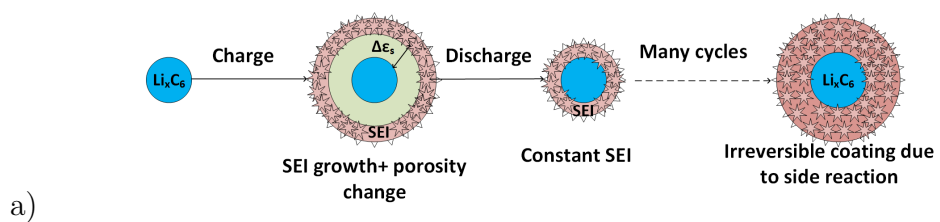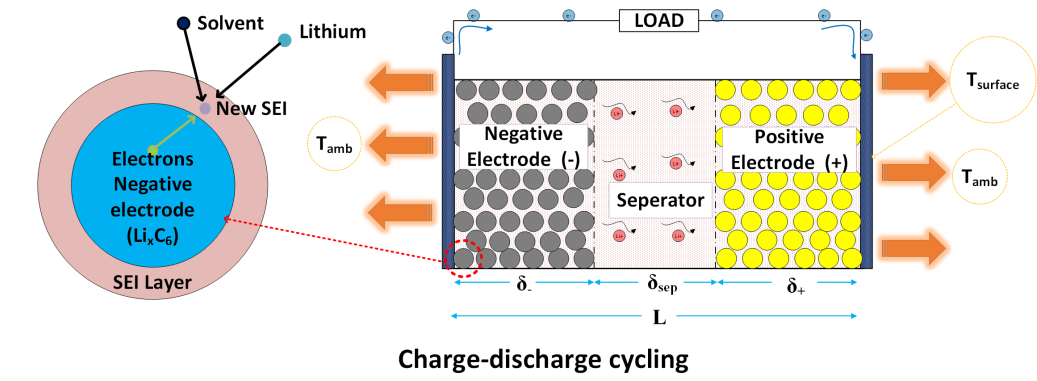$$\left.\frac{\partial c_s}{\partial r}\right|_{r=0} = 0.$$

Figure 1: a) Graphic illustration of the battery model during charge and discharge, and b) flow chart for solution algorithm.

2.1.3. Solid phase potential

The solid phase potential, ϕ_s, is directly proportional to the reaction current density according to Ohm's law.

$$\nabla \cdot (\sigma_{eff} \nabla \phi_s) = (J_1 + J_s). \tag{3}$$

The charge or discharge current is carried by the solid porous material at both electrodes. The reaction current density at the first node (near both current collectors) is made equal to the charge or discharge current density, and the solid potential is evaluated accordingly. At the electrode separator interface, there is no flux of charge, and the zero gradient boundary condition is applied.

$$\sigma_{eff} \frac{\partial \phi_s}{\partial x}\bigg|_{x=0} = \sigma_{eff} \frac{\partial \phi_s}{\partial x}\bigg|_{x=L} = -\frac{I_{app}}{A},$$

$$\frac{\partial \phi_s}{\partial x}\bigg|_{x=\delta_-} = \frac{\partial \phi_s}{\partial x}\bigg|_{x=\delta_+} = 0.$$

2.1.4. Electrolyte phase potential

The electrolyte phase potential, ϕ_e, is evaluated as a function of the reaction current density (J) and the concentration of lithium (c_e) :

$$\nabla \cdot (\kappa_{eff} \nabla \phi_e) + \nabla \cdot (\kappa_{D,eff} \nabla \ln(c_e)) + J_1 + J_s = 0. \tag{4}$$

The effective ionic conductivity, κ_{eff}, is calculated from the Bruggeman relation $\kappa_{eff} = \kappa \varepsilon_e^P$. Using the concentrated solution theory, the effective diffusion conductivity, $\kappa_{D,eff}$, is given:

$$\kappa_{D,eff} = \frac{2RT\kappa_{eff}}{F} \left(t^+ - 1\right) \left\{ 1 + \frac{d \ln f^{\pm}}{d \ln c_e} \right\}.$$

The zero gradient boundary condition is applied at the current collector electrode interface.

$$\frac{\partial \phi_e}{\partial x}\bigg|_{x=0} = 0, \quad \frac{\partial \phi_e}{\partial x}\bigg|_{x=L} = 0.$$

8

2.1.5. Equation for variable porosity

The governing equation for variable porosity can be derived from overall material balance. The electrolyte phase porosity is related to the partial molar concentration and the current density: [22].

$$\frac{\partial \varepsilon_e}{\partial t} = a_s(J_1 V_{Li^+} + J_s V_{Lac}).$$ (5)

The inter-facial surface area to volume ratio for a particle with radius Λ_s is calculated by the following equation [13].

$$a_s = 3\varepsilon_s/\Lambda_s.$$ (6)

Please note that the change in radius of the spherical particle due to the porosity change is not considered in this model.

2.1.6. Intercalation and solvent reduction reaction current density

All the above equations; lithium in electrolyte (equation 1), lithium in solid phase (equation 2), solid potential (equation 3), electrolyte potential (equation 4) are coupled together by the Butler-Volmer equation [2].

$$J_1 = a_s i_o \left\{ \exp\left(\frac{\alpha_n F \eta}{RT}\right) - \exp\left(-\frac{\alpha_p F \eta}{RT}\right) \right\},$$ (7)

where i_o is the exchange current density which is proportional to the solid state lithium concentration (c_s) and electrolyte lithium concentration (c_e). The solid concentration is taken from the surface of a spherical particle (the outermost control volume).

$$i_o = k_{ct}(c_s^{max} - c_s^{sur})^{\alpha_n} c_s^{\alpha_p} c_s^{\alpha_n},$$ (8)

where k_{ct} is the kinetic rate constant, adjusted in such a way to match the initial current density of $3.6 \times 10^{-3} \text{Acm}^{-2}$ at the negative electrode and $2.6 \times 10^{-3} \text{Acm}^{-2}$ at the positive electrode.

In the present model, the SEI layer forms a uniform coating over the solid particle during charge and the thickness of the SEI layer remains unchanged during discharge. In

9

this study, the capacity fading is assumed to occur due to the continuous solvent reduction side reaction, and other phenomena such as graphite cracking, gas generation electrolyte decomposition, SEI precipitation, dendrite growth and lithium plating are not included in this study [25, 26, 27].

The solvent reduction reaction kinetics is similar to the intercalation reaction and can be represented by a similar expression:

$$J_s = a_s i_{os} \left\{ \left(\frac{c_p}{c_p^*} \right) e^{(\alpha_a f \eta_s)} - \left(\frac{c_s}{c_s^*} \right) \left(\frac{c_{Li+}}{c_{Li+}^*} \right) e^{(\alpha_c f \eta_s)} \right\}.$$

5 The above equation can be reduced to a much simpler form using the cathodic Tafel approximation [9] by considering the reaction irreversible.

$$J_s = -a_n i_{os} e^{(-\alpha_c f \eta_s)}. \tag{9}$$

This equation assumes that the SEI layer adds resistance to the negative electrode, while the SEI layer does not affect the positive electrode overpotential. The resistance due to SEI layer increases during charge while it remains constant during discharge [9].

The empirical correlation for OCV at the negative and positive electrodes is taken from Smith and Wang [13]. Over potential positive electrode:

$$\eta_p = \phi_s - \phi_e - U_p.$$

Over potential negative electrode:

$$\eta_n = \phi_s - \phi_e - U_n - J \frac{G_{film}}{a_n}.$$

The overpotential for side reaction is defined as:

$$\eta_s = \phi_s - \phi_e - U_{ref} - J \frac{G_{film}}{a_n}.$$

The reference voltage, U_{ref}, is taken as zero in all calculations.

The battery is assumed to start with the initial resistance, Ω_{SEI}. The resistance of the SEI layer is estimated by the conductivity values available in literature [9]. The SEI layer thickness keeps increasing over charge cycles and the overall resistance at any cycle is calculated as

$$G_{film} = \Omega_{SEI} + \frac{\delta_{film}}{\kappa_p}.$$

The rate of SEI layer increase over a particular cycle is proportional to the solvent reduction reaction current density.

$$\frac{\partial}{\partial t}\delta_{film} = -\frac{J_s M_p}{a_n \rho_p F}.$$

For each cycle the thickness increases over time according to

$$\delta_{film}\Big|_N = \delta_{film}\Big|_{N-1} + \delta_{film}(t). \tag{10}$$

2.1.7. Thermal modelling

The energy balance for the battery heat generation is given by: [15]

$$\rho C_p \frac{\partial T}{\partial t} = \lambda \frac{\partial^2 T}{\partial x^2} + Q_{react} + Q_{rev} + Q_{ohm}. \tag{11}$$

5 where Q_{react} is the heat generation due to reaction inside the battery, Q_{rev} is the reversible heat generation and Q_{ohm} is the Ohmic heat generation rate. Each term in equation 11 is defined as follows:

$$
\begin{aligned}
Q_{react} &= J\left(\phi_s - \phi_e - U\right), \\
Q_{rev} &= TJ\frac{\partial U}{\partial T}, \\
Q_{ohm} &= \sigma_{eff}\left(\frac{\partial \phi_s}{\partial x}\right) + \kappa_{eff}\left(\frac{\partial \phi_e}{\partial x}\right)^2 + \frac{2\kappa_{eff}RT}{F}(1 - t_+^0)\frac{\partial \ln ce}{\partial x}\frac{\partial \phi_e}{\partial x}.
\end{aligned}
\tag{12}
$$

Total heat generated inside the battery is convected to the ambient.

$$-\lambda \frac{\partial T}{\partial x}\bigg|_{x=0} = h(T_{amb} - T),$$
$$-\lambda \frac{\partial T}{\partial x}\bigg|_{x=L} = h(T - T_{amb}).$$

2.1.8. Temperature dependency of properties

All the battery properties are temperature dependent, and change in temperature will affect the physiochemical property ψ following the Arrhenius correction [13].

$$\psi = \psi_{ref} \exp\left[\frac{E_{act}^{\psi}}{R}\left(\frac{1}{T_{ref}} - \frac{1}{T}\right)\right]$$

The reference temperature is $T_{ref} = 298.15$ K and the activation energy (E_{act}) for each parameter is given in Table 2.

5 *2.2. Solution method and flow chart*

The governing equations are discretised using a finite volume method with a collocated approach of all electro-chemical variables defined at the control volume centre. The equations are solved in a sequential way. A fully implicit method is used in this formulation. All simulation parameters were chosen from preliminary simulations. A grid independency test

10 was carried out to decide the number of grid points. The present model uses 20 control volumes at the negative electrode, 15 at the separator, and 25 at the positive electrode. Each solid spherical particle is again divided radially into 25 control volumes. A time step size of one second is used. The current densities for the main reaction and solvent reduction reaction are calculated at each time step. The solution algorithm is explained in Figure

15 1b. Inner iterations are provided to enhance coupling between equations. Proper under-relaxation is employed for the system of equations. The governing equations for electrolyte concentration (equation 1), solid potential (equation 3) and electrolyte potential (equation 4) are solved at the nodal point corresponding to the centre of the control volume, while the solid concentration (equation 2) is solved at radial nodes at each cartesian nodal point.

12

	Negative Electrode	Separator	Positive Electrode
Parameters for Base Battery Model, Smith and Wang (2006)			
Thickness, δ	50×10^{-4}	25.4×10^{-4}	36.4×10^{-4}
Particle radius, Λ_s	1×10^{-4}		1×10^{-4}
Active material volume fraction ε_s	0.580		0.500
Electrolyte phase volume fraction ε_e	0.332	0.5	0.330
Maximum solid phase concentration c_s^{max}	16.1×10^{-3}		23.9×10^{-3}
Stoichiometry at 0% SOC	0.126		0.936
Stoichiometry at 100% SOC	0.676		0.442
Average electrolyte concentration c_e	1.2×10^{-3}	1.2×10^{-3}	1.2×10^{-3}
Exchange current density (i_o)	3.6×10^{-3}		2.6×10^{-3}
Charge-transfer coefficients α_a, α_c	0.5, 0.5		0.5, 0.5
SEI layer film resistance, Ω_{SEI} [1]	100		100
Solid phase Li diffusion coefficient, D_s	2.0×10^{-12}		3.7×10^{-12}
Solid phase conductivity, σ	1.0		0.1
Electrolyte phase Li^+ diffusion coefficient, D_e	2.6×10^{-6}	2.6×10^{-6}	2.6×10^{-6}
Bruggeman porosity exponent, p	1.5	1.5	1.5
Electrolyte activity coefficient, $f^{\pm}$	1.0	1.0	1.0
Li^+ transference number, t_+^0	0.363	0.363	0.363
Parameters for solvent reduction side reaction, Ramadass et al. (2004)			
Reference voltage U_{ref} [1]	0		0
Molecular weight M_p	7.3×10^4		
Density of SEI Layer ρ_p	2.1×10^{-3}		
Side reaction exchange current density i_{os} [1]	1.5×10^{-12}		
Conductivity of SEI Layer κ_p [1]	1×10^{-4}		
Parameters for thermal model, Maleki et al. (1999) & Wu et al. (2013)			
Density of electrolyte ρ_e	1123.0×10^6	1123.0×10^6	1123.0×10^6
Density of solid phase ρ_s	1347.3×10^6		2328.5×10^6
Electrolyte thermal Conductivity λ_e	3.39×10^{-2}	3.39×10^{-2}	3.39×10^{-2}
Solid phase thermal conductivity λ_s	3.39×10^{-2}		3.39×10^{-2}
Heat capacity C_p	1437.4	1978.2	1669.2
Electrolyte heat capacity		2055.1	
Parameters for variable porosity, Sikha et al. (2004)			
Partial molar volume for main reaction V_{Li^+}	13.0		
Partial molar volume for side reaction V_{Lac}	64.39		

Table 1: Electro-chemical modelling parameters of 6Ah battery.

	Negative Electrode	Separator	Positive Electrode
Exchange current densities, E^{io-}, E^{io+}	3×10^4		3×10^4
Solid phase diffusion coefficient , E_{act}^{Ds-}, E_{act}^{Ds+}	4×10^4		2×10^4
Electrolyte phase diffusion coefficient , E_{act}^{De}	1×10^4	1×10^4	1×10^4
Electrolyte phase conductivity , E_{act}^{κ}	2×10^4	2×10^4	2×10^4

Table 2: Activation energies for the Arrhenius correction [13]

	V_{Li+}	V_{Lac}	First cycle charging time(s)
Constant porosity	0.0	0.0	64.77
Variable porosity	13.0	64.39	59.61
Variable porosity	40.0	64.39	50.15
Accelerated porosity	13.0	100.0	59.61

Table 3: Assumed partial molar concentration of the electrolyte $LiPF_6$

The battery is started from the 100% depth of discharge (DoD) condition and charged until the upper cut-off voltage (UCV) is reached. The UCV is taken as 4.0 V in all simulations except the validation study, where 3.9V is used. It has been observed that the SEI layer grows at a much faster rate for overcharging conditions. Hence the UCV is kept at a slightly overcharged condition of 4.0V in this study to accelerate the SEI layer growth. The discharge simulation starts by reversing the applied current until the lower cut-off voltage (LCV) is reached. The LCV is taken as 3.3V in all simulations except the validation study, where 3.29V is used. The DoD is measured with stoichiometry of the positive electrode. However, the negative stoichiometry also shows excellent agreement with values presented in Table 1 at 0% and 100% DoD. This process describes one complete cycle of battery operation. The sign convention applied in this paper is that a positive current discharges the battery. The reaction current density at the negative electrode during discharge is taken as positive.

Battery operating parameters such as voltage and temperature are calculated at the end of each time step. Both voltage and temperature can be completely decoupled from the main electro-chemical governing equations and are not incorporated inside the main loop. The porosity is updated at the beginning of each time step. The equations are iterated in
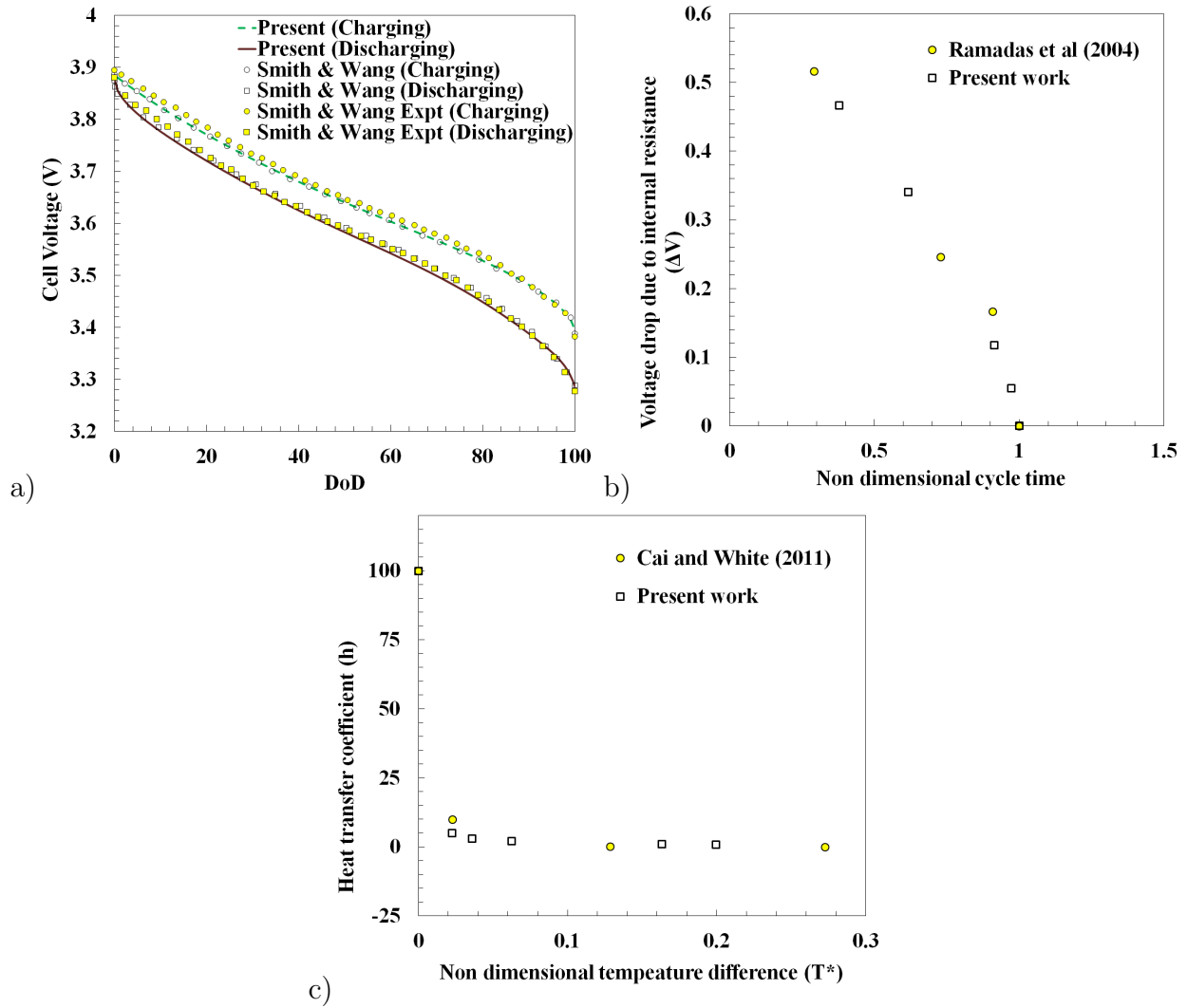
Figure 2: Model validation. a) Electro-chemical model validation with Smith & Wang (2006), b) capacity fade model comparison with Ramadass *et al.* (2004), and c) thermal model comparison with Cai & White (2011).

a coupled way until the residual error reduces below a threshold value. The convergence criteria for current densities on both electrodes are 10^{-3} A/cm^3.

2.3. Validation study

A through evaluation was provided in this study for the electro-chemical model, capacity fade model and thermal model, separately. A validation study was performed to compare the present results with available data in literature. Figure 2a shows a validation study for the

15

base electro-chemical model [13]. The cell is charged from 100% DoD up to the UCV, and the discharge simulation starts from 0% DoD until the LCV. A sharp decrease in discharge near 80% DoD is due to the low diffusion of ions in the solid phase. Between 20% DoD and 80% DoD, it exhibits a balance between the Li^+ ions liberated from the negative electrode and the ions consumed at the positive electrode. The characteristics shown in Figure 2a are in excellent agreement with Smith & Wang [13].

The capacity fade model results are compared with Ramadass $et\ al.$ [28]. It is observed that the cell negative electrode resistance increases with cycling, resulting in a sudden change in voltage at the beginning of charge and discharge. Figure 2b presents the voltage drop (ΔV) plotted against the non dimensional cycle time. The voltage drop is measured as the difference between the UCV and the available voltage after charge-discharge cycle. The non-dimesional time is calculated based on the first cycle time assuming that the first cycle is free from all parasitic side reactions. The results show an excellent agreement with the trends observed in Ramadass $et\ al.$ [28].

The thermal model results are compared with Cai and White [15]. Figure 2c shows the variation of heat transfer coefficient with non-dimensional temperature on the battery surface. The control volumes near the current collector represent the surface temperature of the battery. The temperature increase (ΔT) is calculated based on the ambient temperature. The non-dimensional temperature is defined as $T^* = \frac{T_{max} - T_{amb}}{T_{amb}}$. The temperature is observed to rise to a higher value at the beginning of charge and discharge and then it reaches an equilibrium with the ambient condition. The trend presented in Figure 2c shows an excellent agreement with Cai and White [15].

3. Results and Discussion

3.1. Effect of variable porosity on battery performance

This section analyses the dependency of variable porosity on the battery performance. The variable porosity equation links the battery performance with electrolyte properties. Figure 3a shows the effect of different partial molar volumes for both the main and parasitic
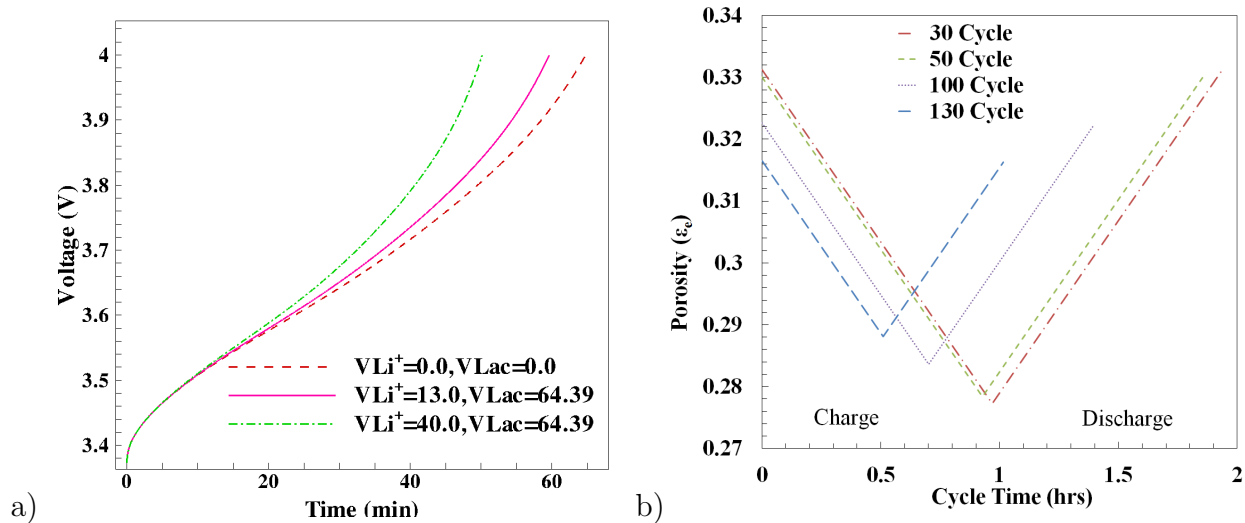
16

Figure 3: Variable porosity studies for 1C (6A-CC) charge and discharge. a) Battery charging performance comparison with different molar volume, and b) variation of porosity for $V_{Li^+} = 13.0$ and $V_{Lac} = 64.39$ showing irreversible filling due to solvent reduction side reaction.

reaction (V_{Li^+} and V_{Lac}) on charging performance of the battery. Please note that these simulations are performed with an isothermal condition (298.15K), removing the effect of any thermal expansion on porosity change. Figure 3a shows a comparison of variable porosity cases. The case with $V_{Li^+} = 0$ and $V_{Lac} = 0$ corresponds to the constant porosity condition. The intercalation molar volumes (V_{Li^+}) varied from 13 to 40, while keeping the constant partial molar concentration for the parasitic reaction at $V_{Lac} = 64.39$ (see table 3).

The case with zero partial molar concentrations results in no porosity change and hence the available area for reaction remains constant, resulting in longer cell operating time. In this case, the charging time extends up to 65 minutes and the capacity of the battery is the highest compared to the other two cases. The case with a higher V_{Li^+} shows a faster decrease in porosity, subsequently reducing the specific interfacial surface area available for reaction. A lower specific interfacial surface area a_s also decreases the current density of the intercalation reaction (equation 7) and solvent reduction reaction (equation 9). With $V_{Li^+} = 40$, the cell charging is limited to 50 minutes of operation and the cell capacity reduces for both charging and discharging operations. The decrease in current density also affects indirectly the full system of equations and imposes a considerable damping effect on the

17

overall chemical reaction, reducing the solid phase (ϕ_s) and electrolyte phase (ϕ_e) potentials.

Figure 3b quantifies the irreversible filling of pores in the negative electrode. This figure shows the variation in porosity at the negative electrode and current collector interface over a period of 30 to 130 charge-discharge cycles. The case for $V_{Li^+} = 13$ and $V_{Lac} = 100$ is used to keep the large irreversible change in porosity. The initial electrolyte porosity at the negative electrode is taken as $\varepsilon_e = 0.332$ (Table 1) and after 130 cycles of operation the porosity reduces to $\varepsilon_e = 0.315$. This irreversible filling effect can be explained as follows.

The variable porosity contributions are from the intercalation reaction and solvent reduction side reaction. The porosity variation in a lithium ion battery is proportional to the product of current density and partial molar volumes (equation 5). The porosity contribution from intercalation reaction is usually ignored in capacity fade study since this is completely reversible, whereas the solvent reduction side reactions are not. The change in porosity due to charge cycle is cancelled out in the subsequent discharge cycle in case of an intercalation reaction. There is irreversible filling in the negative electrode due to the solvent reduction side reaction which is activated only in the charge cycle and absent in the discharge cycle. The porosity variation in the positive electrode is reversible since the electrode is free from the side reaction. Hence this variable porosity model is able to capture the irreversible plugging of pores with the solvent reduction side reaction which is one of the main causes of accelerated capacity fade during cycling.

The combined effect of the change in porosity and the SEI layer growth is responsible for the capacity fade in a battery. The porosity variation limits the available area and fills the pores irreversibly as shown in figure 3b. These changes are negligible during early cycles of operation and the battery behaves almost like a new battery. This observation was made for SONY 18650 battery, operating under similar conditions and experimentally tested by Ramadass *et al.* [28]. In this study, the partial molar concentration is set to be $V_{Li^+} = 13$ for the intercalation reaction and $V_{Lac} = 64.39$ for the side reactions to limit the battery operation close to 60 minutes as per the manufacturer specification.
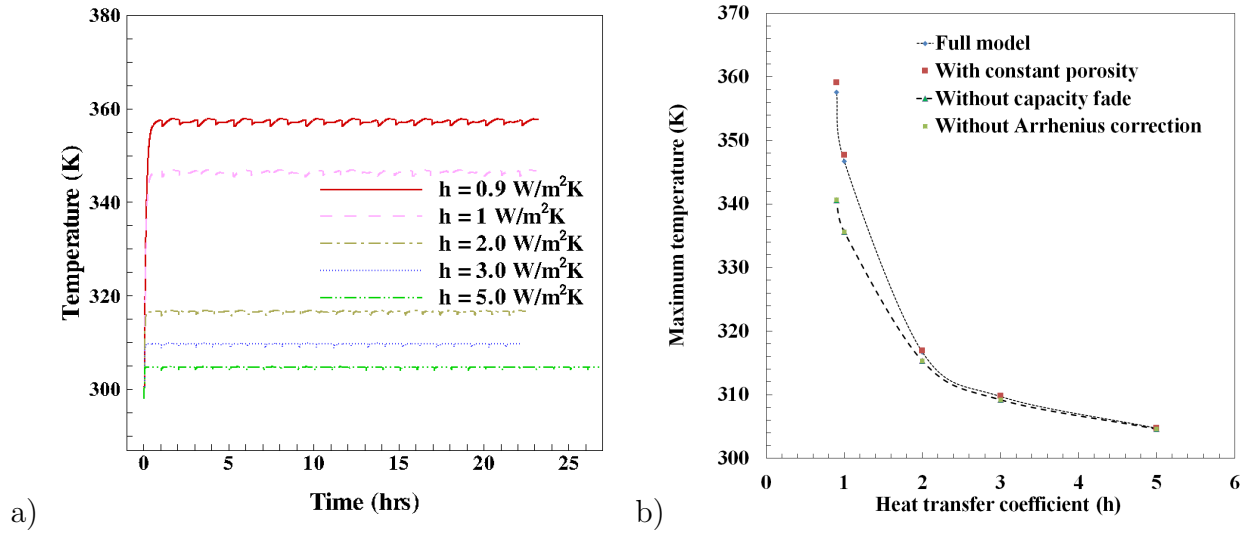
18

Figure 4: Thermal performance of the battery under 1C (6A CC)cyclic loading. a) Battery thermal performance inclusive of all sub models, and b) effect of individual sub models on battery thermal performance.

3.2. Effect of temperature on battery performance

Figure 4a shows the temperature variation for the first few cycles, plotted at the battery surface with different heat transfer coefficients. The node temperature corresponding to both electrode current collector interfaces, is taken as the surface temperature. This figure ₅ presents the temperature variation of the battery including the effects of capacity fading, variable porosity and the Arrhenius correction. The heat generation inside the battery has main contributions from Ohmic heat generation Q_{ohm} and reaction heat generation Q_{react}, and comparatively less from reversible heat Q_{rev} (see equation 13). The ohmic heat Q_{ohm} is due to the limited internal conductivity and this term accounts for the ohmic heat in the ₁₀ solid phase as well as the electrolyte phase [13]. There is a sharp increase in temperature during the initial phase of the charge cycle and subsequently the battery reaches a balance between the internal heat generation and the heat convected outside. There is a small decrease in temperature when the battery changes from a charge cycle to a discharge cycle. This is visible in all different heat transfer cases presented in Figure 4a, and could be due ₁₅ to comparatively reduced contribution of the internal heat generation (Q_{ohm} and Q_{react}) at the beginning of charge or discharge process. For a perfect natural convection case, the heat

19

transfer coefficient is nearly 5 W/m^{2}K and temperature of the battery remains at 305K, well below the runaway temperature. An increase in battery temperature can be observed with a decrease in convective heat transfer coefficient.

Figure 4b shows the effect of various sub models on the battery thermal performance. The variable porosity model does not affect the overall surface temperature of the battery significantly. This could be due to the fact that the overpotential (η) remains almost unaffected and mainly contributes to the ohmic heat generation (Q_{ohm}) and the reaction heat generation (Q_{react}). Also, the capacity fade solvent reduction side reaction does not have much influence on the temperature profile during the initial cycles of operation. The contribution of the solvent reduction reaction current density is much smaller than that of the intercalation current density, and its influence on the reaction heat generation (Q_{react}) and the reversible heat generation (Q_{rev}) is negligible. Also the side reaction has no significant influence on the solid phase potential (ϕ_s) and the electrolyte phase potential (ϕ_e) at the start of a battery. The thermal contribution of the solvent reduction reaction changes after the SEI layer becomes thick. A high temperature accelerates the capacity fade in a battery and causes the cell to fail at an early stage compared to a properly cooled battery. This effect is captured in the following figure by analysing the rate of the SEI layer growth with different heat transfer coefficients.

It is interesting to note that the Arrehenius correction plays a significant role in deciding the performance of a battery by influencing the physiochemical variables ψ. The solid phase diffusion coefficient and exchange current density affect the charge transfer resistance, thus enabling the lithium to diffuse through the solid phase at a much faster rate and improving the performance of a battery with a temperature increase [14].

Figure 5 shows the battery life with different heat transfer coefficients. For $h = 0.9$ W/m^{2}K, the battery operates at a comparatively high temperature of 357K and the battery life is short and the rate of the SEI layer growth is high. The battery operating time is measured as the time up to the breakdown point where the current flux balance is no longer satisfied and the battery is no longer usable. For a heat transfer coefficient of $h = 5.0$
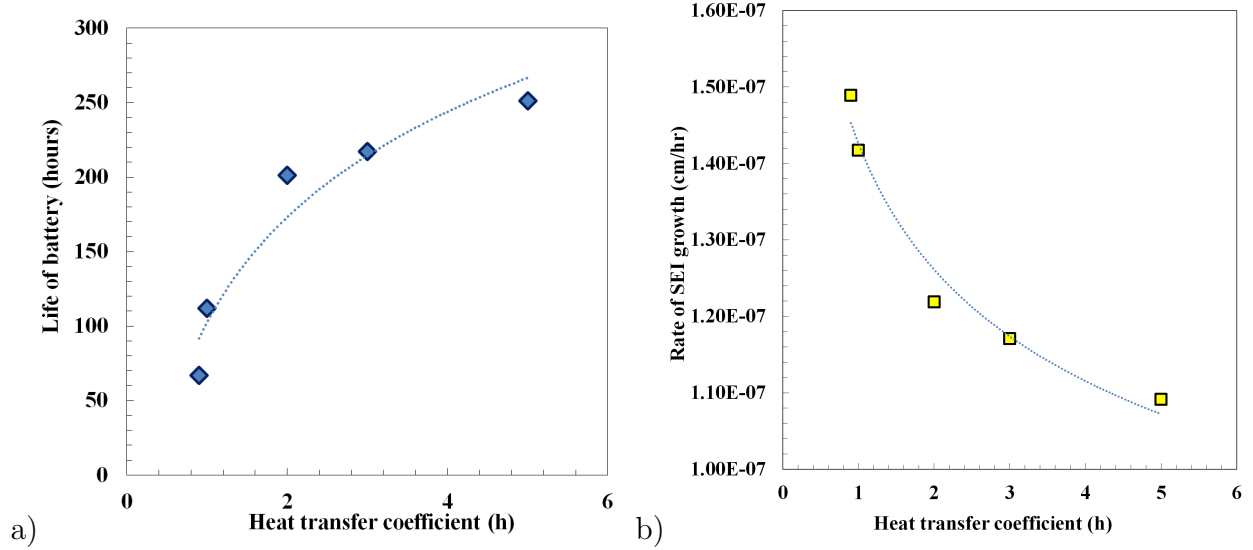
20

Figure 5: Dependency of heat transfer coefficient on 1C (6A-CC) charging and discharging. a) Operating time of battery with different heat transfer coefficient, and b) rate of SEI growth with different heat transfer coefficient.

W/m^2K the rate of the SEI layer growth is low and the battery operates for more than 250 hours. The higher the heat transfer coefficient is, the lower the rate of the SEI layer growth is and the longer a battery operates.

As shown in Figure 5a, the battery operating temperature is inversely proportional to the heat transfer coefficient. High temperature influences the battery electrolyte and solid phase diffusivity and changes the exchange current density considerably. The important parameter is the diffusivity (D_e) of lithium through electrolyte and the SEI layer which is linked to the operating temperature by the Arrhenius expression. Also the temperature has an indirect effect on the SEI layer growth through the solid potential (ϕ_s) and electrolyte potential (ϕ_e) and hence the overpotential for the solvent reduction reaction (η_s). Increasing the heat transfer coefficient from $h = 0.9W/m^2K$ to 2 W/m^2K results in a major improvement, whereas increasing the heat transfer coefficient from $h = 3W/m^2K$ to 5 W/m^2K gives a modest improvement. The $h = 5$ W/m^2K case is very close to the iso-thermal condition where the heat transfer coefficient is infinite. In this condition, the battery life is determined by the SEI layer growth due to cycling. Other capacity fade mechanisms which are not

21

included in this study are explained in Xu [27].

The rate of the SEI layer growth can be approximated by the following correlation for a given set of modelling parameters

$$\frac{d\delta_{film}}{dt} = 1.0 \times 10^{-7} h^{-0.177}.$$

The life of battery follows the following correlation

$$t_{hours} = 102 \ln h + 102.4$$

These correlations provide an estimate of the dependency of capacity fading parameters and could be useful for designing a cooling system to enhance the battery life. Smith *et al.* [29] shows that at a lower battery temperature, ageing occurs at a much slower rate compared to a higher temperature. The observed temperature dependency shows that high temperature increases the rate of capacity fade and can contribute to accelerated ageing. The capacity fade of a battery is also dominated by the diffusivity of multiple species through the SEI layer. Capacity fade can be reduced by limiting products with high diffusivity [10]. This is captured in the present model using conductivity of electrolyte (κ) through the SEI layer. Most of these effects can be controlled by adjusting κ values.

3.3. Effect of capacity fade on battery performance

Figure 6 shows the cyclic operation of a battery at different operating times. The solid line shows the profile with the capacity fading effect while the dotted line shows without the capacity fading effect. This analysis is conducted with constant porosity under an iso-thermal condition. The exchange current density for solvent reduction reaction and other parameters are summarised in Table 1. For the first few hours of operation as shown in Figure 6a, the profiles show an almost identical trend, and the internal resistance of the cell is almost the same as the initial SEI layer resistance of $\Omega_{SEI} = 100 \ \Omega\text{cm}^2$. The SEI layer starts growing over the subsequent charge cycles and it becomes significant after multiple cycles of operation. The loss of active material contributes to a decrease in battery capacity
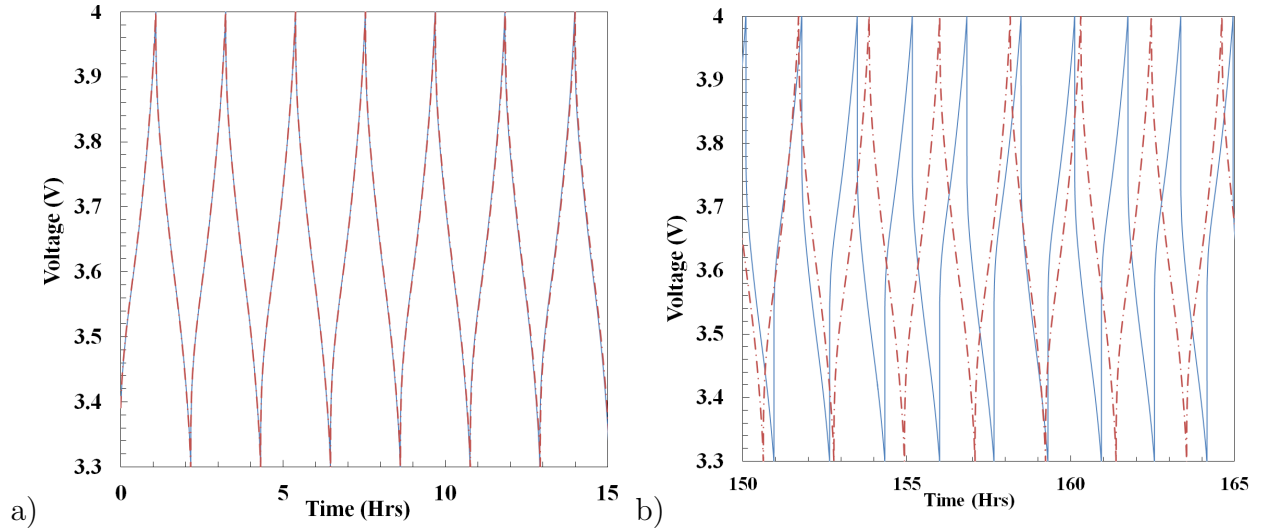
22

Figure 6: Battery operation with and without capacity fading effect. a) Voltage profile for the first 15 hours of operation, and b) voltage profile after 150 hours of operation.

over cycles. In this study, the solvent reduction reaction exchange current density (i_{os}) is found to be a significant parameter influencing the cell capacity fade and overall performance. The value of i_{os} is chosen to be high so that the cell capacity reduces to less than a half after 100 cycles of operation. For all other analysis, $i_{os} = 1.5 \times 10^{-12}$ is used unless otherwise specified.

Figure 6b shows the cycle operation of cell after 150 hours of operation with a significant SEI layer built up. The charge and discharge cycle becomes much shorter with the capacity fade model. There is certainly a phase difference for cases with capacity fade while comparing with cases without capacity fade. This phase shift is absent at the beginning of battery operation and increases gradually. The internal resistance causes a cycle time reduction and affects the battery operating parameters and current density. Due to the SEI Layer built up, the externally applied voltage has to reach a certain value to overcome the internal resistance to continue the charging operation. A similar effect can be observed at the beginning of the discharge cycle where the available voltage is lost to overcome the internal resistance.

The important variables affecting the battery capacity are the LCV (or end-of-charging voltage, EOCV), the UCV (or end-of-discharge voltage, EODV), and the DoD. The battery
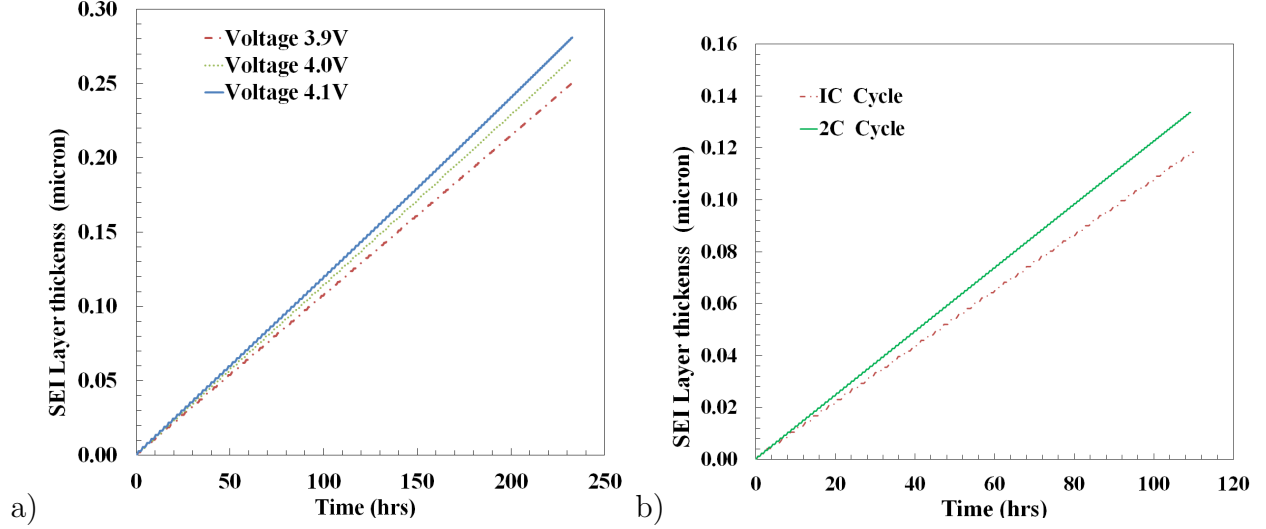
23

Figure 7: Cell operating characteristics with different operating conditions. a) SEI growth with different UCV, and b) SEI growth with different C-rates.

is subjected to different overcharging conditions with three UCV values of 3.9V, 4.0V and 4.1V. The SEI layer growth is observed and the voltage profile is analysed in each case. Due to the safety concerns, manufacturers do not recommend for charging above the UCV. Figure 7a shows that even a slight overcharging of 0.1V accelerates the SEI layer growth.

5 In a similar study, Ramadass *et al.* observed that increasing the UCV by 0.1V reduced the battery life by 60% [9]. The lower the UCV is, the shorter the time takes to reach the UCV. The time taken to reach 3.9V is shortest among the three cases. The maximum rate of the SEI layer growth is observed for 4.1V. This is due to the change in overpotential for the side reaction (η_n) which affects the SEI layer growth for different cut off voltages. At UCV

10 limits, the overpotential for the solvent reduction side reaction becomes large compared to the normal operating conditions, causing the dominance of $a_n i_{os}$ term in equation 9. During the normal operating conditions, the side reaction current density is much smaller compared to $a_n i_{os}$ due to the dominance of $\exp^{(-\alpha_c f \eta_s)}$. So, the capacity loss increases by increasing the cut off potentials, and it accelerates the SEI layer growth compared to the normal operating

15 conditions. A similar capacity fade effect can be observed for lower LCV values.

Figure 7b shows the battery operating at a higher C-rate. The SEI layer growth rate
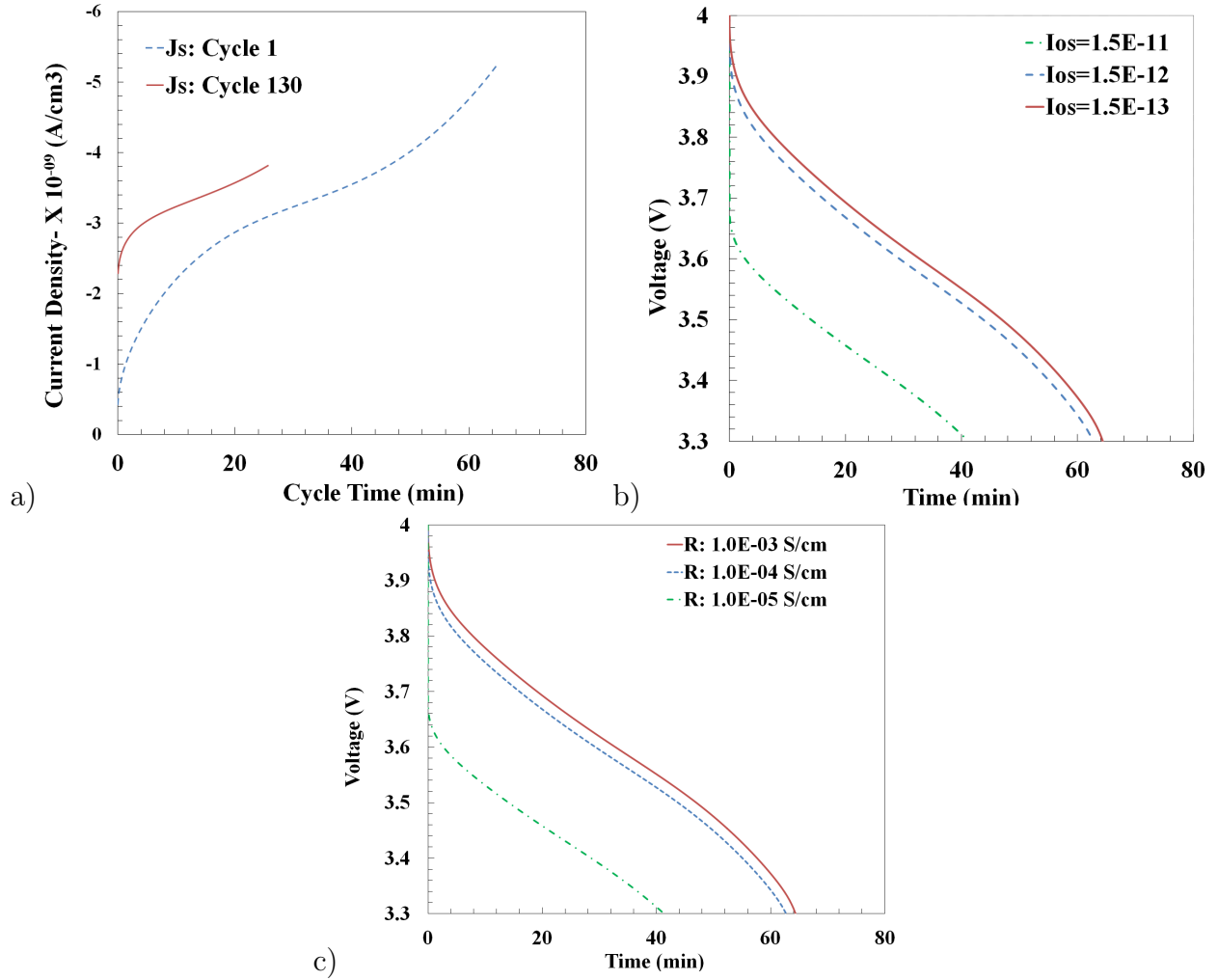
24

Figure 8: Cell performance after multiple charge-discharge cycles. a) Solvent reduction current density at negative current collector interface, b) voltage profiles with different i_{os} values after 30 cycles, and c) voltage profiles with different κ_p values after 30 cycles.

changes with C-rate, and high current charging and discharging accelerates the SEI layer growth. The high charge/discharge rate increases the current density in a battery which is directly proportional to the side reaction overpotential (η_n) and the SEI layer growth (δ).

Figure 8a shows variations in solvent reduction current density at the negative electrode current collector interface. During the first charge cycle the current density variation extends to a large range. After 130 cycles of charge/discharge, the range of variation diminishes to less than a half. This is due to a gradual built up of internal resistance where the overpotential

25

term for the solvent reduction reaction $\eta_n = \phi_s - \phi_e - U_n - (J_1 + J_s)\frac{G_{film}}{a_n}$ is dominated by the contribution from the side eaction current and the film resistance. The exponential term in $J_s = -a_n i_{os} e^{(-\alpha_c f \eta_s)}$ becomes very small due to a high value of overpotential, and the variation in side reaction current density is limited to a smaller range. This shows that after a sufficient build up of internal resistance, the solvent reduction reaction is mainly dominated by the combined contributions from a_n and i_{os}. The same effect can be seen while the battery is kept idle, without being connected to the external load. Thus η_s reduces to zero and the non-operating time SEI growth is governed by the exchange current density and specific area. Hence this model is capable of predicting the idle time SEI layer growth of battery. Combining this capacity fade model with the variable porosity model can accurately predict the idle and non-idle time SEI growth because the porosity model can calculate the specific area accurately.

Figure 8b shows the cell performance after 30 cycles of operation with different values of side reaction exchange current density (i_{os}) for capacity fade. Different values of i_{os} are used in this study to analyse the effect of capacity fade. It is important to find the correct i_{os} value for accurate capacity fade modelling. The i_{os} value remains constant throughout the simulation and cannot be modified at the start of each cycle. Increasing i_{os} accelerates the side reaction, hence reducing the cell life significantly. The case of $i_{os} = 1.5 \times 10^{-11}$ shows that the cell life reduces below 45 minutes after 30 cycles of operation.

Figure 8c shows the cell performance with different values of SEI layer conductivity (κ_p). This conductive layer is formed over the solid spherical particles due to solvent reduction side reaction which appears as a coating, preventing solid particles from further reaction. For $\kappa_p = 1.0 \times 10^{-3}$ S/cm, the battery operates for 65 minutes whereas the battery capacity is slightly reduced for $\kappa_p = 1.0 \times 10^{-4}$ S/cm. Case of $\kappa_p = 1.0 \times 10^{-5}$ S/cm shows a significant reduction in the capacity compared to other cases where the battery operates only for 42 minutes under a similar operating condition. Thus less conductive products formed during the side reaction reduce the battery life significantly. There is a threshold value for κ_p, below which the battery performance deteriorates substantially. Thus it is critical to estimate the

value of i_{os} and κ_p for the capacity fade analysis of the Li-ion battery. Appropriate values of i_{os} and κ_p depend mainly on the choice of electrolyte.

4. Conclusion

Capacity fade of lithium-ion batteries under cyclic loading conditions has been modelled.
5   The capacity fade modelling considers the thickness of the SEI layer formed over the solid particle in the negative electrode during charge. An electro-chemical model is demonstrated to capture most of the significant electro-chemical effects inside the battery under cyclic charge and discharge conditions. The operating characteristics and the battery life are governed by electro-chemical reactions including the capacity fading, thermal effects and active
10   surface area of the electrode. Sensitivity studies are performed to identify the important parameters affecting the battery life. It is found that multiple factors affect the performance and the battery life, most of which are interlinked. The SEI layer forms the irreversible coating preventing the chemical reaction. This is captured by linking the model to the partial molar concentration. This is again linked with the operating temperature which is a function
15   of the convective heat transfer coefficient. The model can be used as an optimisation tool to enhance the performance and the battery life under various operating conditions. This model enables the operator to choose a safe operating limit for the battery while minimising the SEI layer growth.

5. Acknowledgement

Nomenclature

a	active surface area per electrode unit volume (cm^{-1})
A	Electrode plate area (cm^2)
c	Volume-averaged concentration ($\mathrm{mol\,cm}^{-3}$)
C_p	Specific heat ($\mathrm{J\,kg}^{-1}\,\mathrm{K}^{-1}$)
D	Diffusion coefficient ($\mathrm{cm}^2\,\mathrm{s}^{-1}$)
E	Activation energy ($\mathrm{J\ mol}^{-1}$)
F	Faradays constant, 96,487 $\mathrm{C\,mol}^{-1}$
G	Resistance ($\Omega\,\mathrm{cm}^2$)
h	Convective heat transfer coefficient ($\mathrm{W\,m}^2\,\mathrm{K}^{-1}$)
i_o	Exchange current density for intercalation reaction ($\mathrm{A\,cm}^{-2}$)
i_{os}	Exchange current density for solvent reduction reaction ($\mathrm{A\,cm}^{-2}$)
I_{app}	Applied current (A)
J_1	Reaction current for intercalation reaction ($\mathrm{A\,cm}^{-3}$)
J_s	Reaction current for solvent reduction reaction ($\mathrm{A\,cm}^{-3}$)
k_{ct}	Kinetic rate constant for intercalation reaction
L	Cell width (cm)
M_p	Molecular weight ($\mathrm{kg\,mol}^{-1}$)
Q	Heat generation ($\mathrm{W\,cm}^{-3}$)
r	Radial coordinate (cm)
R	Universal gas constant, 8.3143 ($\mathrm{J\,mol}^{-1}\,\mathrm{K}^{-1}$)
t	Time (s)
t_+^0	Transference number
T	Absolute temperature (K)
U	Open-circuit potential(V)
V	Cell voltage (V)
V	Partial molar volume ($\mathrm{cm}^3\,\mathrm{mol}^{-1}$)
w	Stoichiometric ratios in positive and negative electrode
x	Coordinate along the cell width (cm)
y,z	Stoichiometric coefficient in chemical reaction

Greek Symbols

α	Charge-transfer coefficient
δ	Thickness (cm)
ϵ	Volume fraction of domain
ρ	Density ($\mathrm{kg\,cm}^{-3}$)
κ	Conductivity of electrolyte ($\mathrm{S\,cm}^{-1}$)
κ_D	Diffusivity ($\mathrm{A\,cm}^{-1}$)
κ_p	Conductivity of SEI layer ($\mathrm{S\,cm}^{-1}$)
Λ_s	Radius of particle (cm)
λ	Thermal conductivity ($\mathrm{W\,cm}^{-1}\,\mathrm{K}^{-1}$)
σ	Solid phase conductivity ($\mathrm{S\,cm}^{-1}$)
ϕ	Volume averaged potential (V)
Ω_{SEI}	Initial resistance of SEI layer ($\Omega\,\mathrm{cm}^2$)

Superscript & subscript

amb	Ambient condition
e	Electrolyte phase
eff	Effective
$film$	SEI layer thickness
i	Electrodes
max	Maximum
n	Negative electrode
N	Cycle number
ohm	Ohmic
p	Positive electrode
ref	Reference values
react	Reaction
rev	Reversible
s	Solid phase of positive or negative electrode
sur	Surface quantity
$-$	To the left of an interface
$+$	To the right of an interface

List of Figures

[1] M. Doyle, T. F. Fuller, J. Newman, Journal of the Electrochemical Society 140 (1993) 1526–1533.

[2] M. Doyle, J. Newman, Journal of Power Sources 54 (1995) 46–51.

[3] C. Wang, W. Gu, B. Liaw, Journal of the Electrochemical Society 145 (1998) 3407–3417.

[4] V. R. Subramanian, J. A. Ritter, R. E. White, Journal of The Electrochemical Society 148 (2001) E444–E449.

[5] T.-S. Dao, C. P. Vyasarayani, J. McPhee, Journal of Power Sources 198 (2012) 329–337.

[6] A. Bizeray, S. Duncan, D. Howey, et al., in: Hybrid and Electric Vehicles Conference 2013 (HEVC 2013), IET, IET, pp. 1–6.

[7] R. Spotnitz, Journal of Power Sources 113 (2003) 72–80.

[8] H. J. Ploehn, P. Ramadass, R. E. White, Journal of The Electrochemical Society 151 (2004) A456–A462.

[9] P. Ramadass, B. Haran, P. M. Gomadam, R. White, B. N. Popov, Journal of the Electrochemical Society 151 (2004) A196–A203.

[10] M. B. Pinson, M. Z. Bazant, Journal of the Electrochemical Society 160 (2013) A243–A250.

[11] A. V. Randall, R. D. Perkins, X. Zhang, G. L. Plett, Journal of Power Sources 209 (2012) 282–288.

[12] T. R. Tanim, C. D. Rahn, Journal of Power Sources 294 (2015) 239–247.

[13] K. Smith, C.-Y. Wang, Journal of Power Sources 160 (2006) 662–673.

[14] B. Wu, V. Yufit, M. Marinescu, G. J. Offer, R. F. Martinez-Botas, N. P. Brandon, Journal of Power Sources 243 (2013) 544–554.

[15] L. Cai, R. E. White, Journal of Power Sources 196 (2011) 5985–5989.

[16] M. Guo, R. E. White, Journal of Power Sources 221 (2013) 334–344.

[17] Y. Ye, Y. Shi, N. Cai, J. Lee, X. He, Journal of Power Sources 199 (2012) 227–238.

[18] S. Chacko, Y. M. Chung, Journal of Power Sources 213 (2012) 296–303.

[19] A. Barai, K. Uddin, W. Widanalage, A. McGordon, P. Jennings, Journal of Power Sources 303 (2016) 81–85.

[20] J. Yi, U. S. Kim, C. B. Shin, T. Han, S. Park, Journal of Power Sources 244 (2013) 143–148.

[21] U. S. Kim, C. B. Shin, S. M. Chung, S. T. Kim, B. W. Cho, Journal of Power Sources 190 (2009) 184–188.

[22] G. Sikha, B. N. Popov, R. E. White, Journal of The Electrochemical Society 151 (2004) A1104–A1114.

[23] T. F. Fuller, M. Doyle, J. Newman, Journal of the Electrochemical Society 141 (1994) 1–10.

[24] H. Maleki, S. Al Hallaj, J. R. Selman, R. B. Dinwiddie, H. Wang, Journal of The Electrochemical Society 146 (1999) 947–954.

[25] J. Vetter, P. Novák, M. Wagner, C. Veit, K.-C. Möller, J. Besenhard, M. Winter, M. Wohlfahrt-Mehrens, C. Vogler, A. Hammouche, Journal of power sources 147 (2005) 269–281.

[26] P. Verma, P. Maire, P. Novák, Electrochimica Acta 55 (2010) 6332–6341.

[27] K. Xu, Chemical reviews 114 (2014) 11503–11618.

[28] P. Ramadass, B. Haran, R. White, B. N. Popov, Journal of power sources 112 (2002) 606–613.

[29] A. Smith, J. Burns, D. Xiong, J. Dahn, Journal of The Electrochemical Society 158 (2011) A1136–A1142.